ARTICLE

Check for updates

Lightweight and High-Performance Microwave Absorber Based on 2D WS$_2$–RGO Heterostructures

Deqing Zhang[1,6], Tingting Liu[1], Junye Cheng[2] ✉, Qi Cao[3,4], Guangping Zheng[5], Shuang Liang[1], Hao Wang[2] ✉, Mao-Sheng Cao[6] ✉

Deqing Zhang and Tingting Liu have contributed equally to this work.

✉ Junye Cheng, jycheng4-c@my.cityu.edu.hk; Hao Wang, whao@szu.edu.cn; Mao-Sheng Cao, caomaosheng@bit.edu.cn

[1] School of Materials Science and Engineering, Qiqihar University, Qiqihar 161006, People's Republic of China

[2] Guangdong Provincial Key Laboratory of Micro/Nano Optomechatronics Engineering, College of Mechatronics and Control Engineering, Shenzhen University, Shenzhen 518060, People's Republic of China

[3] Department of Chemistry, School of Science, The University of Tokyo, Tokyo 113-8656, Japan

[4] Department of Mechanical Engineering, School of Engineering, The University of Tokyo, Tokyo 113-8656, Japan

[5] Department of Mechanical Engineering, Hong Kong Polytechnic University, Hung Hom, Kowloon, Hong Kong, People's Republic of China

[6] School of Materials Science and Engineering, Beijing Institute of Technology, Beijing 100081, People's Republic of China

HIGHLIGHTS

- WS$_2$–rGO nanosheets with ultra-small thicknesses and ultra-lightweight, were successfully prepared by a facile hydrothermal method.

- The WS$_2$–rGO isomorphic heterostructures exhibited remarkable microwave absorption properties.

ABSTRACT Two-dimensional (2D) nanomaterials are categorized as a new class of microwave absorption (MA) materials owing to their high specific surface area and peculiar electronic properties. In this study, 2D WS$_2$–reduced graphene oxide (WS$_2$–rGO) heterostructure nanosheets were synthesized via a facile hydrothermal process; moreover, their dielectric and MA properties were reported for the first time. Remarkably, the maximum reflection loss (RL) of the sample–wax composites containing 40 wt% WS$_2$–rGO was −41.5 dB at a thickness of 2.7 mm; furthermore, the bandwidth where RL < −10 dB can reach up to 13.62 GHz (4.38–18 GHz). Synergistic mechanisms derived from the interfacial dielectric coupling and multiple-interface scattering after hybridization of WS$_2$ with rGO were discussed to explain the drastically enhanced microwave absorption performance. The results indicate these lightweight WS$_2$–rGO nanosheets to be potential materials for practical electromagnetic wave-absorbing applications.

KEYWORDS 2D WS$_2$ nanosheets; Reduced graphene oxide; Heterostructure; Microwave absorption
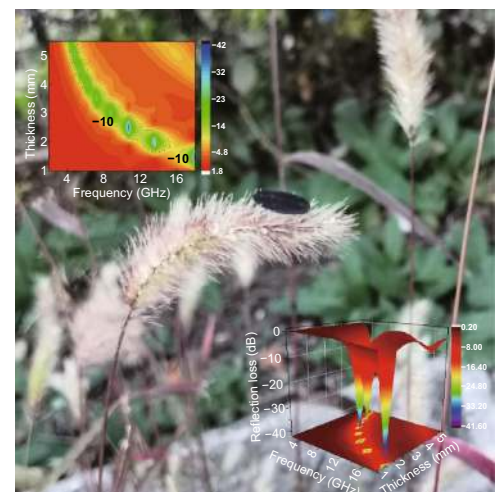
1 Introduction

The rapid development of modern industries has highlighted the significance of and the urgent need for developing high-performance electromagnetic wave absorbents with strong absorption, large bandwidth, small thickness, low density, and high temperature/corrosion resistance. Nonetheless, the use of single-component and conventional absorbing materials is not adequate to satisfy the social and industrial requirements [1–7]. Therefore, substantial efforts have been devoted to exploiting novel absorbing materials; these the two-dimensional (2D) materials with ultrathin-layered structures have attracted significant attention owing to their large surface areas and unique electronic properties [8–15]. For example, molybdenum disulfide (MoS_2), a transition metal dichalcogenide (TMD), has a layered structure similar to that of graphite [16–19]. MoS_2 nanosheets [20, 21] obtained via the top-down exfoliation method have been reported to exhibit remarkable dielectric properties and absorption performance owing to the dipole polarization at defective sites (*e.g.*, Mo and S vacancies) and ultra-large surface area [22, 23]. In addition to the characteristics of 2D materials [24], such as the quantum and finite-size effects as well as surface and boundary effects, these exhibit high chemical stability and electrical conductivity. The electronic properties of TMDs can be varied from metallic to semiconducting by modulating the crystal structure or layer numbers; this further indicates their substantial potential for application in microwave absorption. However, 2D transition metal sulfides exhibit low electrical conductivity and may not achieve the most suitable impedance matching. It is challenging for single-component dielectric materials to achieve satisfactory microwave absorption performance without being coupled with other dielectric or magnetic components. Thus, introducing the second component into TMD-based absorbents appears significant for further enhancement in their microwave absorption properties [25–27].

Recently, carbon materials [28] including carbon nanotubes (CNTs) [29–32], carbon fibers, and other carbon nanocomposites [33–35] have also been widely investigated for microwave absorption owing to their favorable properties such as low densities and high complex permittivity. Considering this, reduced graphene oxide (rGO) is likely to be an effective complementary material [36]. In a previous work, it was reported that an rGO/CNTs composite with a three-dimensional (3D)

nanoarray structure exhibited remarkable microwave absorption performance [37]. Moreover, a composite paper composed of Co_3O_4 nanocubes and rGO, when used as microwave absorbent, achieved a maximum reflection loss (RL) of -31.7 dB at a thickness of 2.5 mm [38]. In addition, a solvothermal-synthesized MoS_2/rGO heterostructure nanosheet absorber has been reported to exhibit a maximum RL of -31.57 dB at a thickness of 2.5 mm [39]. Similarly, WS_2–rGO heterostructure nanosheets could also be synthesized by the solvothermal method [34]; these nanosheets have been used for electrocatalytic hydrogen evolution [40–43]. However, the dielectric loss and microwave absorption properties of WS_2–rGO systems have not been studied.

In this work, WS_2–rGO heterostructure nanosheets are synthesized and are used as microwave absorbers for the first time. The coupling of WS_2 with rGO, which results in the formation of WS_2–rGO heterostructure nanosheets, is demonstrated to be a facile approach for dramatically improving the microwave absorption performance of WS_2; it yields a maximum RL of -41.5 dB at 9.5 GHz with a thickness of 2.7 mm, and a large effective bandwidth of 3.5 GHz with a thickness of 1.7 mm. Based on the systematic structural characterization and electromagnetic measurements, the mechanisms responsible for the superior performances of those heterostructures are proposed. The thin and lightweight WS_2–rGO heterostructure nanosheet composites in conjunction with their facile synthesis route indicate the numerous potential for developing novel lightweight and high-performance microwave absorption devices.

2 Experimental Details

2.1 Materials

All the reagents were of analytical grade and used without further purification. Tungsten hexachloride (WCl_6) was obtained from Aladdin Industrial Corporation. Thioacetamide (CH_3CSNH_2) was supplied by Tianjin Guangfu Fine Chemical Research Institute. Graphene oxide (GO, concentration: 2 mg/mL) was supplied by Xianfeng Nano. Hydrazine hydrate ($NH_2 \cdot NH_2 \cdot H_2O$, content $\geq 50\%$) was obtained from Shenyang Xinxi Reagent Plant. Anhydrous ethanol was obtained from Tianjin Tianli Chemical Reagent Co., Ltd. Deionized water was obtained from Qiqihar City Tianyiyuan Water Plant.

2.2 Preparation of WS$_2$ Nanosheets

Tungsten chloride (WCl$_6$) (2.0 g) and thioacetamide (4.0 g) were added to 75 mL of deionized (DI) water. The mixture solution was stirred for 30 min and then transferred to a polyphenylene (PPL) autoclave (100 mL), which was heated to 210 °C and maintained at this temperature for 20 h. Subsequently, it was cooled down to room temperature naturally. The black precipitate was extracted from the solution by centrifugation, washed several times with DI water and ethanol, and finally dried in vacuum at 60 °C for 12 h. The sample was denoted as pristine WS$_2$ nanosheets and used for comparison with the WS$_2$–rGO heterostructure nanosheets.

2.3 Preparation of Reduced Graphene Oxide (rGO)

To obtain rGO, a graphene oxide (GO) dispersion was sonicated for 2 h. Then, hydrazine hydrate was added dropwise to the GO dispersion at room temperature. The reduction was performed at 100 °C for 1 h. The weight ratio of 9:7 for hydrazine hydrate and GO was applied to prepare the sample. The resulting black precipitate was filtered using a filtering paper and washed with anhydrous ethanol and DI water till a neutral pH was attained. Finally, the filtrated precipitate was dried at room temperature for 24 h. The sample was denoted as rGO and used for comparison with the WS$_2$–rGO heterostructure nanosheets.

2.4 Preparation of WS$_2$–rGO Heterostructure Nanosheets

The WS$_2$–rGO heterostructure nanosheets were prepared by a one-pot hydrothermal method. Briefly, 1.5 g of WCl$_6$, 3.5 g of thioacetamide, and 30 mL of GO dispersion (2 mg mL^{-1}) were mixed; then, DI water was added, achieving a total volume of 75 mL. The mixture solution was stirred for 30 min and then transferred to a 100-mL PPL autoclave, which was heated to 210 °C and maintained at this temperature for 20 h. Subsequently, it was naturally cooled down to room temperature. The resulting black precipitate was recovered from the solution by centrifugation, washed several times with DI water and ethanol, and finally dried in vacuum at 60 °C for 12 h. The sample was denoted as WS$_2$–rGO heterostructure nanosheets.

2.5 Characterizations

The morphology and crystal structure of the as-synthesized products were characterized by transmission electron microscopy (TEM, Hitachi, H-7650) and high-resolution TEM (HRTEM, FEI, Tecnai F30). X-ray photoelectron spectroscopy (XPS) analysis was carried out on an X-ray photoelectron spectrometer (ESCALAB250Xi, Thermofisher Co). The X-ray diffraction (XRD) patterns were recorded using a German Bruker-AXS D8 X-ray diffractometer with Cu-K$_\alpha$ radiation ($\lambda = 0.1541$ nm). Raman spectroscopy measurements were conducted on a LabRAM HA Evolution system. The defects of the material were analyzed by electron paramagnetic resonance (EPR, Bruker, ER200-SRC-10/12) and fluorescence spectrometer (PL, Hitachi, F7000). The absorption properties of the as-synthesized product were characterized using an ultraviolet spectrophotometer (UV–Vis, PE Company, Lambda 750). The specific surface area and pore size of the WS$_2$–rGO heterostructure nanosheets were analyzed using a specific surface area and void analyzer (BET, Quantachrome, NOVA 2000E). The thickness of the as-synthesized product was analyzed by atomic force microscopy (AFM, Bruker, Dimension Edge). The electromagnetic absorption characteristics of the sample were determined by a coaxial method using a vector network analyzer (VNA, MS4644A Anritsu) in the frequency range of 2–18 GHz. Typically, a mixture containing 40 wt% of the as-prepared WS$_2$–rGO heterostructure nanosheets and 60 wt% wax was prepared and compressed using a mold to form a ring with an inner diameter of 3 mm and an outer diameter of 7 mm. A 2-mm-thick coaxial center ring was used to evaluate the electromagnetic wave absorption characteristics.

3 Results and Discussion

3.1 Morphological, Structural, and Phase Characterization

In order to identify the phase and crystal structure of the WS$_2$–rGO heterostructure nanosheets, characterization based on XRD and Raman spectrum was performed. The results are shown in Fig. 1. In Fig. 1a, several apparent diffraction peaks at $2\theta = 14.2°$, $33.6°$, $39.5°$, and $59.0°$ could be identified; these correspond to the crystal planes of (002), (101), (103), and (110), respectively, of WS$_2$. These peak positions are reasonably consistent with those of the WS$_2$ standard card (PDF No. 08-0237), demonstrating the phase

purity of WS_2 in the as-synthesized product. In the XRD patterns of the WS_2–rGO heterostructure nanosheets, the additional peak corresponding to the (002) planes of rGO appears at $2\theta = 24.1°$ as compared to that of pristine WS_2. Moreover, it is observed in Fig. S1A that the characteristic peak of pristine rGO also appears at $2\theta = 24.1°$, indicating that the rGO was doped into WS_2 successfully. It is apparent that the positions of the main diffraction peaks of WS_2 do not change, except that the intensity of the peak at $2\theta = 14.2°$ corresponding to the (002) planes of WS_2 decreases evidently. The XRD results indicate that the addition of rGO could have significantly suppressed the stacking of the (002) planes of WS_2 during the solvothermal process; this could have consequently promoted the formation of ultrathin 2D layers of WS_2 [44, 45]. Meanwhile, owing to the introduction of rGO, the intensity of each diffraction peak of the composite material is weakened. It could have been caused by the introduction of rGO, resulting in the increases in defect density and hence the deterioration of the crystal quality of WS_2.

The successful formation of WS_2–rGO compounds was also revealed by Raman spectroscopy. The Raman spectrum of the WS_2–rGO heterostructure nanosheets (shown in Fig. 1b) displays two characteristic peaks at 1356 and 1598 cm^{-1}; these are compared with that of the pristine rGO (Fig. S1B). The ratio of the intensities of the D- and G- bands (I_D/I_G) is commonly used to estimate the degree of structural defects in reduced graphene oxides; in this work, it is calculated to be 1.05, which is significantly higher than that of rGO ($I_D/I_G = 0.94$). The results indicate the presence of a large number of dangling bonds and defects in the rGO after complexation with WS_2. Moreover, distinct E_{2g} and A_{1g} peaks for WS_2 are observed at 355 and 421 cm^{-1}. The blueshift in the A_{1g} mode can be attributed to the increase in the van der Waals interactions between the layers. Meanwhile, the anomalous behavior of the E_{2g} mode can be attributed to the strong dielectric screening of the long range Coulombic interactions between the effective charges in the samples. Thus, the XRD and Raman results adequately demonstrate that rGO was successfully incorporated into the 2D WS_2 nanosheets during the one-pot solvothermal reaction [26]. It was also verified by the infrared spectroscopy (Fig. S2) that GO was effectively reduced to rGO and that WS_2 and rGO were effectively combined to form the heterostructures.

A typical TEM image of the as-prepared WS_2–rGO heterostructure nanosheets is presented in Fig. 1e. It is observed that the loading of rGO on WS_2 was uniform as compared to that of pure WS_2 (Fig. 1c) or rGO (Fig. 1d). In those heterostructure nanosheets, rGO retained the wrinkled structure even when it was grown in situ on the surface of WS_2. Meanwhile, WS_2 exhibited a layered, broken cotton-like structure. Notably, this growth process endowed WS_2 nanosheets the maximum contact area with rGO, resulting in a high electrical conductivity of the heterostructure. The conductivity of the heterostructure nanosheet was measured with a four-probe station and observed to be 10 s cm^{-1}; meanwhile, that of pure WS_2 was determined to be 3.33 s cm^{-1}, as listed in Table S1. This indicates that the coupling between WS_2 and rGO could increase the conductivity of the WS_2 nanosheets. In addition, the presence of graphene suppressed the stacking of the (002) planes of WS_2, enabling the WS_2–rGO compounds to grow into relatively thin sheets. Because the interlayer spacing was different across the layered materials, it could be employed to identify the different phases in the heterostructures. As revealed by the HRTEM image and the corresponding selected-area electron diffraction (SAED) patterns (inset of Fig. 1f), the interlayer spacing of approximately 0.62 and 0.31 nm could be indexed to adjacent WS_2 and rGO layers, respectively. Meanwhile, the diffraction rings in the SAED patterns could also be indexed to the (100) and (105) planes of WS_2 as well as the (100) and (110) planes of rGO; this further verified the coexistence of WS_2 and rGO in the heterostructure nanosheets.

In order to further verify the phases, chemical states, and bonding properties of the WS_2–rGO heterostructure nanosheets, XPS analysis was performed (Fig. 2). As anticipated, signals of only W, S, C, and O were detected in the survey spectrum (Fig. 2a). The atomic percentages of W, S, C, and O deduced from the survey spectrum were 12.57%, 24.23%, 53.53%, and 9.67%, respectively. The W:S ratio is very close to 1:2, indicating that the stoichiometric WS_2 was obtained (Fig. S3). The low content of O indicates that GO was effectively reduced to rGO during the solvothermal synthesis process. In addition, as shown in Fig. 2d, the signals resulting from O-bonded C were significantly suppressed in the recorded C 1s spectrum of the heterostructure nanosheets. The results further verified the low O-content in the heterostructures. Furthermore, it was observed that the binding energies of W 4$f_{7/2}$ and W 4$f_{5/2}$ were 31.80 and 34.10 eV, respectively (Fig. 2b). Meanwhile, a weak peak of W 5$p_{3/2}$ could be observed at a higher binding energy of approximately 38.00 eV (Fig. 2b). The binding energies of S 2$p_{3/2}$ and S 2$p_{1/2}$ were measured to be 161.20 and 162.90 eV,
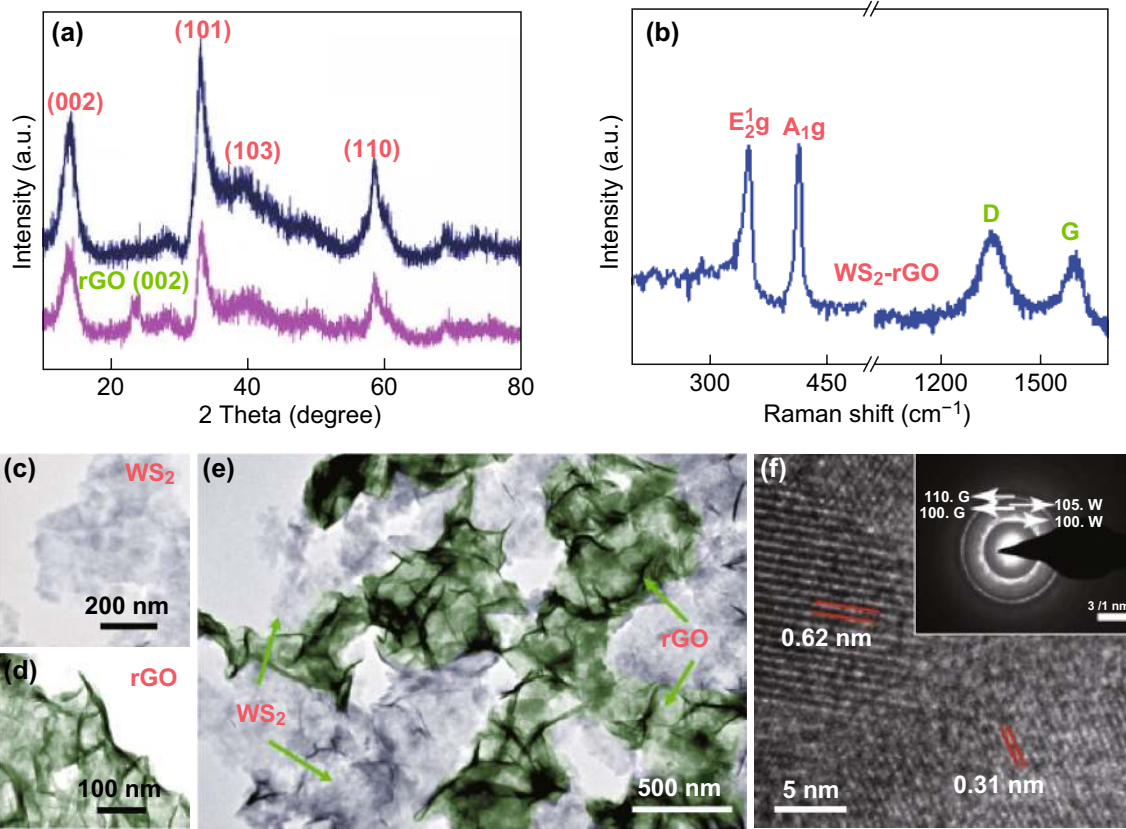
Fig. 1 **a** XRD patterns of WS_2 and WS_2–rGO. **b** Raman spectrum of WS_2–rGO. TEM images of **c** WS_2, **d** rGO, **e** WS_2–rGO. **f** HRTEM image of WS_2–rGO heterostructure nanosheets and the corresponding SAED patterns (inset)

respectively (Fig. 2c). All the binding energy values are in good agreement with the standard values; they further demonstrate the presence of W and S in the chemical states of W^{4+} and S^{2-}, respectively [43].

3.2 Dielectric Properties

To investigate the dielectric properties of the as-prepared WS_2 and WS_2–rGO, dielectric frequency spectra were measured in the frequency range of 2–18 GHz by the coaxial method on an Anritsu MS4644A vector network analyzer. The complex permittivities of WS_2 and WS_2–rGO are shown in Fig. 3. It is evident that after hybridization of WS_2 with rGO, the real permittivity (ε') became higher than that of WS_2. Moreover, the imaginary permittivity (ε'') decreased with increasing frequency. In general, the dielectric loss could be expressed using Debye theory [46], and ε' and ε'' can be described as follows:

$$\varepsilon' = \varepsilon_\infty + \frac{\varepsilon_s - \varepsilon_\infty}{1 + \omega^2 \tau^2} \tag{1}$$

$$\varepsilon'' = \frac{\varepsilon_s - \varepsilon_\infty}{1 + \omega^2 \tau^2} \omega\tau + \frac{\sigma}{\omega\varepsilon_0} \tag{2}$$

where ω is the angular frequency, τ is the polarization relaxation time, ε_s is the static permittivity, and ε_∞ is the relative dielectric permittivity at the high frequency limit.

According to Eq. (1), the decrease in ε' was owing to the increase in ω in the testing frequency range [47]. This phenomenon can be related with the polarization relaxation at the low-frequency range. Particularly, when rGO was not added, ε' of WS_2 was approximately 8.0; moreover, ε' of rGO was approximately 7.0 (Fig. S1C). After the addition of rGO, ε' apparently improved to approximately 14.0. Meanwhile, ε'' also increased from approximately 3.0 to 7.0, and the corresponding decremental attained 70–119% and 30–101%, respectively. The results indicated that the addition of rGO and the consequent heterostructurization
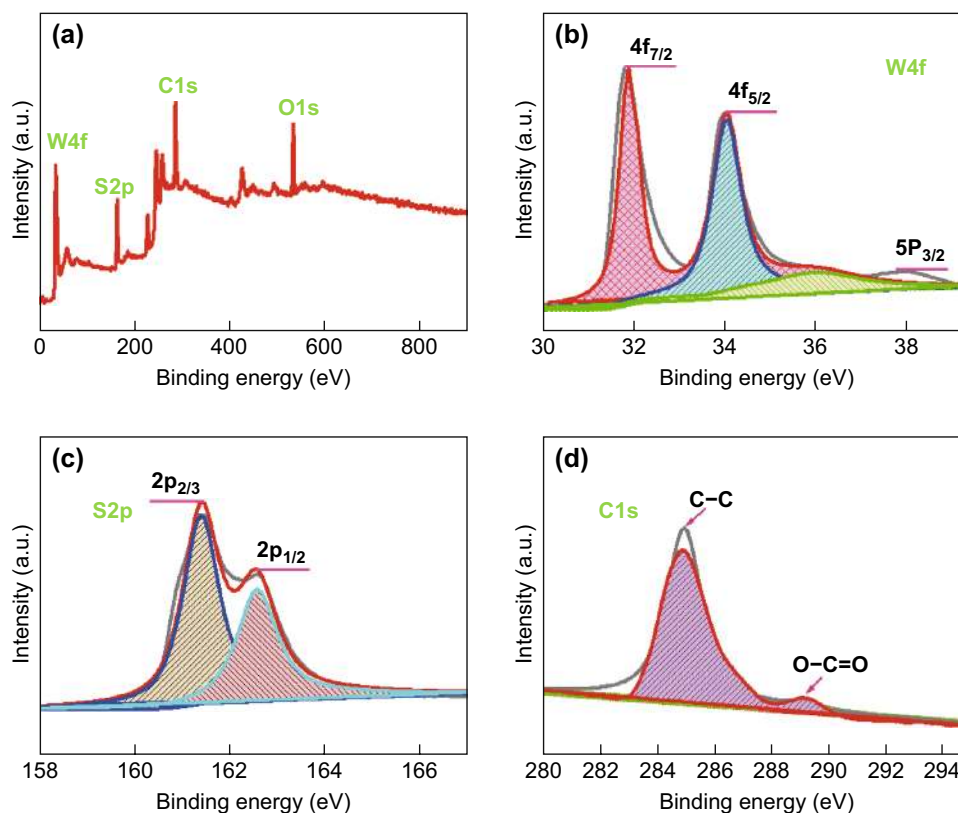
Fig. 2 Typical XPS spectra of as-synthesized WS$_2$–rGO heterostructure nanosheets: **a** XPS wide scan (survey), high-resolution narrow scan on **b** W, **c** S, and **d** C regions in spectra of WS$_2$–rGO

in the WS$_2$–rGO nanosheets significantly improved the dielectric properties of the WS$_2$ nanosheets (Fig. 3a, b); this could be explained by the interfacial polarization in the heterostructures. The interfacial polarization depends on the difference in the conductivity between two components in the heterostructures, which could enhance the dipole polarization [48]. The increases in ε' and ε'' with the increasing loading of rGO could be interpreted rationally according to the effective medium theory. Equation (2) illustrates that ε'' is determined by the polarization and electrical conductivity (σ); moreover, the relaxations in the frequency range of 2–18 GHz were caused by the polarization of defect, as reported previously [49]. The addition of rGO introduced clustered defects and residual bonds during its heterostructurization with WS$_2$; this is likely to have increased the attenuation of electromagnetic waves. Furthermore, because rGO exhibits higher electron mobility, the heterostructures could exhibit a higher hopping conductivity; this in turn

caused strong polarization and the loss of conductance in electromagnetic waves. In addition, the coupling between rGO and WS$_2$ provided more conductive paths for the heterostructures, which substantially increased the dielectric loss as well.

The magnetic permeability profiles of WS$_2$ and WS$_2$–rGO are shown in Fig. 3c, d. It is evident that as compared to the real and imaginary permittivity profiles shown in Fig. 3a, b, the magnetic permeability exhibited negligible change prior to and after the heterostructurization of WS$_2$ and rGO; this indicates that the addition of rGO had no apparent influence on the magnetic properties of WS$_2$. Owing to the absence of magnetism in WS$_2$ and WS$_2$–rGO, u' and u'' were close to one and zero, respectively. u' and u'' were close to one and zero for the pristine rGO as well, as shown in Fig. S1D. In general, the eddy current loss played an important role in the magnetic loss at 2.0–18.0 GHz. u' and u'' are observed to be distinguished from the curve of the standard spectrum, indicating
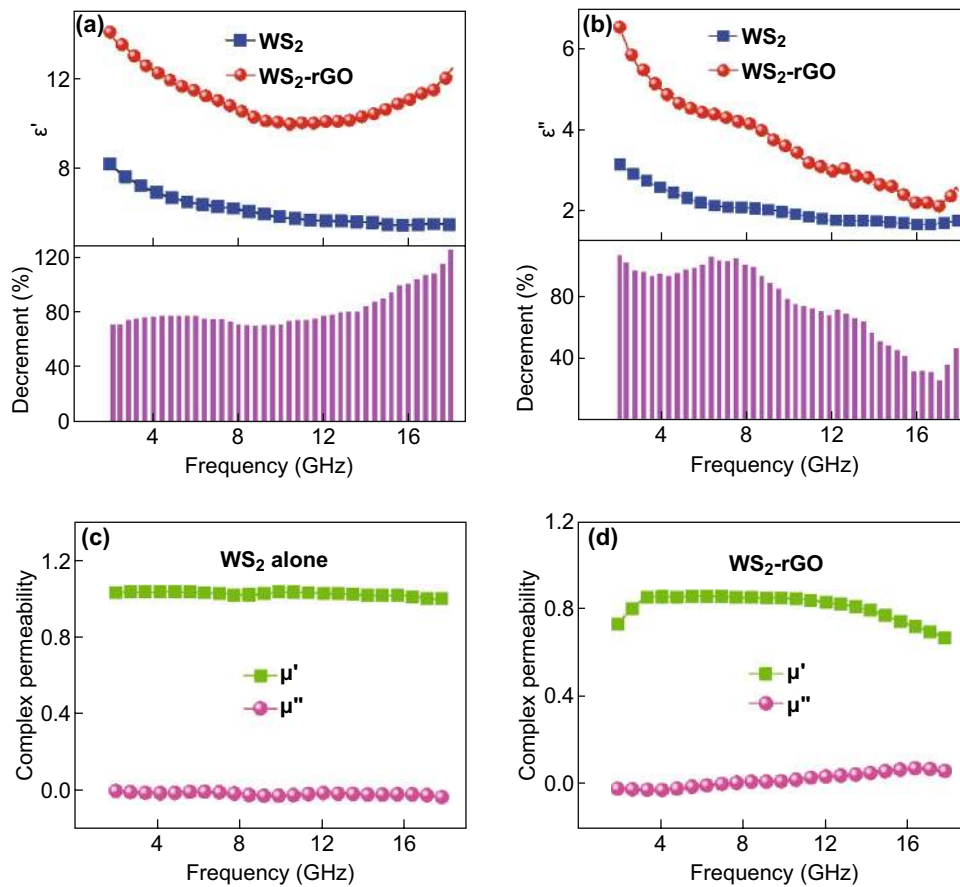
Fig. 3 **a** ε'-curves, and **b** ε''-curves of the as-synthesized WS$_2$ and WS$_2$–rGO. Complex permeability profiles of **c** pure WS$_2$, and **d** WS$_2$–rGO

that the eddy currents were unavoidable. When the magnetic loss is caused only by the eddy current loss, $\mu''(\mu')^{-2}f^{-1}$ does not change with the frequency. The calculated eddy current loss is shown in Fig. 4. It is observed that $\mu''(\mu')^{-2}f^{-1}$ varies with frequency, indicating that the WS$_2$–rGO heterostructure nanosheets attenuated electromagnetic waves by eddy current loss and relaxation. Meanwhile, Fig. 3d shows that μ' and μ'' were very low for the WS$_2$–rGO heterostructure nanosheets. The results thus indicate that the electromagnetic wave absorption property of the WS$_2$–rGO heterostructure nanosheets mainly resulted from the dielectric loss rather than the magnetic loss.

3.3 Microwave Absorption of WS$_2$–rGO

In general, dielectric relaxation could enhance the microwave absorption properties of materials. The reflection loss (RL) of WS$_2$–rGO heterostructure nanosheets was evaluated via Eq. (3) [39]:

$$\text{RL} = 20 \log \frac{|Z_{\text{in}} - Z_0|}{Z_{\text{in}} + Z_0} \tag{3}$$

where the normalized input impedance (Z_{in}) is expressed as Eq. (4):

$$Z_{\text{in}} = \sqrt{\frac{\mu_{\text{r}}}{\varepsilon_{\text{r}}}} \tanh \left[j\frac{2\pi}{c} \sqrt{\mu_{\text{r}}\varepsilon_{\text{r}}}fd \right] \tag{4}$$

where Z_0 is the impedance of air; Z_{in} is the input impedance of the sample; c is the velocity of light; f is the electromagnetic wave frequency; d is the thickness of the absorbent; and ε_{r} and μ_{r} are the complex permittivity and permeability of the composite medium, respectively.

Figure 5 presents the RL curves at different thicknesses for the sample–wax composites containing 40 wt% rGO (Fig. 5a, b), 40 wt% WS$_2$ (Fig. 5c, d), and 40 wt% WS$_2$–rGO heterostructure nanosheets (Fig. 5e, f). The microwave absorption performance of rGO was low, considering that it could exceed the effective absorption of

−10 dB only at a large thickness of 5.5 mm at approximately 18 GHz, with a narrow effective bandwidth of 0.85 GHz (17.15–18 GHz) and maximum RL of −15.8 dB. This is because a remarkable microwave absorbent should exhibit effective electromagnetic attenuation as well as impedance matching characteristics. Although rGO exhibits a high dielectric constant and reasonable electrical conductivity, if its impedance does not match with that of the incident wave, the wave is reflected to the surface of the absorbent, resulting in a weak microwave absorption performance. Therefore, it is very important for the electromagnetic wave-absorbing material to exhibit a suitable impedance matching. Similarly, as shown in Fig. 5c, d, the WS$_2$ nanosheets also exhibited weak absorption, with the effective absorption bandwidth of approximately 13 GHz (5–18 GHz) and maximum RL of −15.5 dB at a large thickness of 5.5 mm. In contrast, as shown in Fig. 5e, f, the microwave absorption properties of the WS$_2$–rGO heterostructure nanosheets are remarkable, with significantly stronger RL than that of the absorbents made only of rGO or WS$_2$ nanosheets. The maximum RL is −25 dB at a thickness of 3.0 mm, and the maximum RL even attains −41.5 dB at a thickness of 1.5 mm. The effective bandwidth is 13.62 GHz (4.38–18 GHz). As listed in Table S2, we compared WS$_2$–rGO with other rGO-based and MoS$_2$-based MA materials reported in the literature. It is observed that WS$_2$–rGO hybrids exhibit remarkable RL values and a broadened bandwidth, indicating the potential applications of WS$_2$–rGO hybrids.

The dramatic enhancement in the microwave absorption properties could have been caused by the hybridization of rGO with WS$_2$, which could regulate the complex
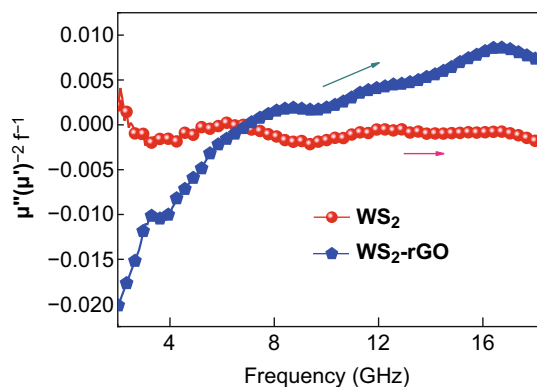

Fig. 4 $\mu''(\mu')^{-2}f^{-1}$ values of WS$_2$ and WS$_2$–rGO at various frequencies

permittivity of WS$_2$ nanosheets. Meanwhile, there were a large number of defects in the WS$_2$ and rGO layers; these were W vacancies and S vacancies in WS$_2$ and a few oxygen-containing functional groups in rGO. These resulted in the generation of a large number of dipoles. As illustrated in Fig. 6a, dipole polarization occurred subsequently; it played an important role in microwave attenuation. In addition, owing to the difference in the conductivity of the surfaces of rGO and WS$_2$, the local charge accumulation and rearrangement could have resulted in interfacial polarization [50–54] under an alternating electromagnetic field. The interfacial polarization sites (Fig. 6b) could be considered as a type of capacitor-like structure and hence could effectively absorb electromagnetic waves. In addition, as shown in Fig. 6c, electrons could absorb the energy of incident microwave and jump among those heterostructure nanosheets, resulting in eddy current losses for microwave attenuation. Moreover, both WS$_2$ and rGO nanosheets exhibited high specific surface area and plenty of interlayer voids owing to their ultrathin 2D structures; this enabled the formation of a favorable multiple-scattering and conductive network (Fig. 6d). Large-scale SEM images (Fig. S4) further reveal the 3D interconnected network structure formed by the WS$_2$–rGO heterostructure nanosheets at micrometer scales; this was also favorable toward enhancing microwave dissipation via the multiple scattering effect. The above-mentioned results demonstrate that the introduction of rGO could significantly improve the wave absorption performance as compared with the pristine tungsten disulfide or rGO. This could be attributed to the differences in impedance matching and attenuation constants, which are two critical parameters that affect the value of RL [55, 56]. In order to achieve zero reflection on the surface of the sample, the characteristic impedance of the sample should be equal to or close to that of the free space, which generally depends on a function between the complex permissibility and complex permeability. A delta-function method was used to validate the degree of impedance matching by Eq. (5) [57–59]:

$$|\Delta| = \left| \sinh^2(Kfd) - M \right| \tag{5}$$

where the values of K and M could be calculated using the complex permittivity and permeability as Eqs. (6) and (7):

$$K = \frac{4\pi\sqrt{\mu'\varepsilon'}}{c\cos\delta_e\cos\delta_m}\sin\frac{\delta_e + \delta_m}{2} \tag{6}$$

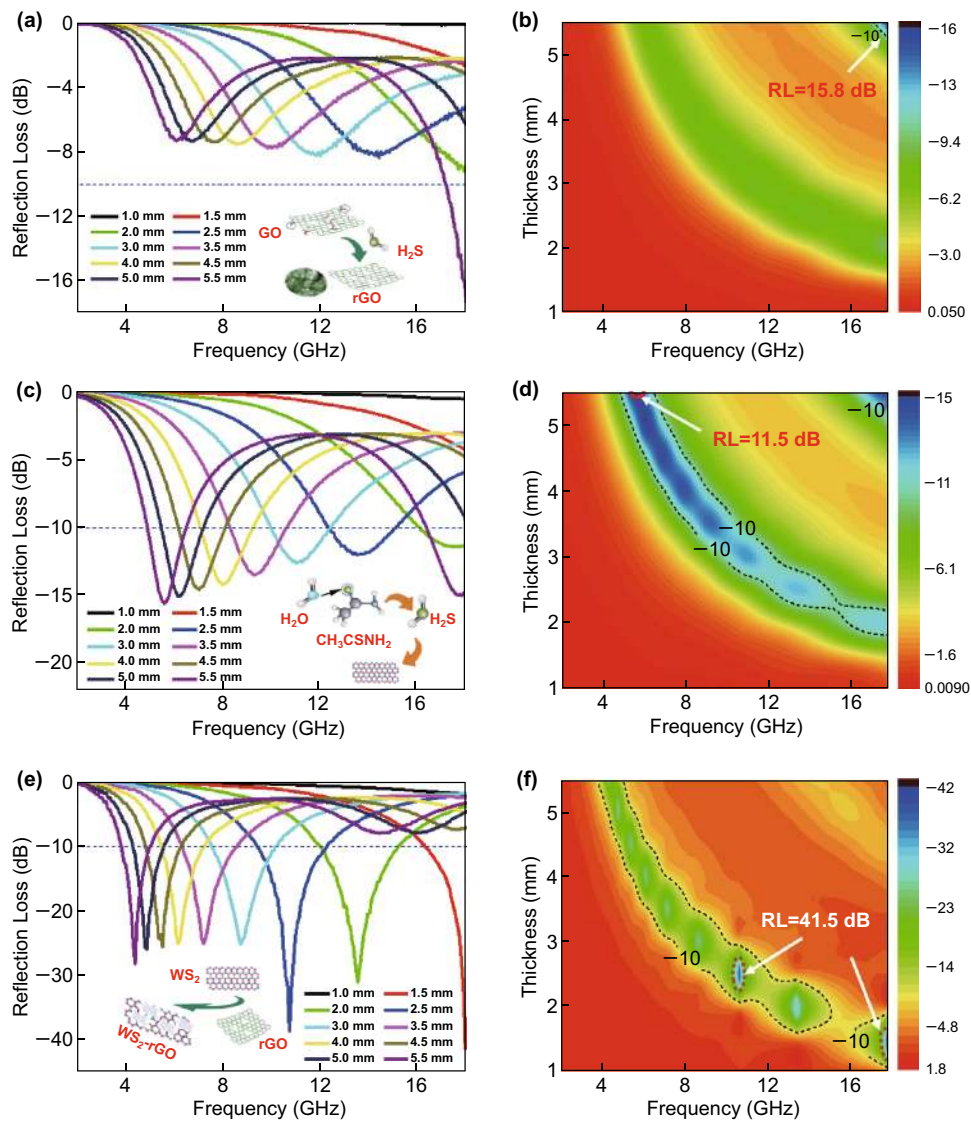**Fig. 5** **a**, **c**, **e** Reflection loss profiles and **b**, **d**, **f** corresponding 2D maps of pure rGO (**a**, **b**), pure WS_2 nanosheets (**c**, **d**), and WS_2–rGO heterostructure nanosheet powder (**e**, **f**). The illustrations in panels **a**, **c**, and **e** represent different preparation processes for pure rGO, pure WS_2, and the WS_2–rGO heterostructure nanosheets, respectively

$$M = \frac{4\mu' \cos \delta_e \varepsilon' \cos \delta_m}{(\mu' \cos \delta_e - \varepsilon' \cos \delta_m)^2 + \left[\tan\left(\frac{\delta_m}{2} - \frac{\delta_e}{2}\right)\right]^2 (\mu' \cos \delta_e + \varepsilon' \cos \delta_m)^2}$$

(7)

Generally, when a smaller |Δ| is obtained, there is a better impedance match between the complex permittivity and complex permeability [60, 61]. The calculated delta value plots for WS_2, rGO, and the WS_2–rGO heterostructure nanosheets at 2–18 GHz are shown in Fig. 7. It is observed that the value for the WS_2–rGO heterostructure nanosheets

is close to zero, indicating a higher impedance matching performance as compared to that of pristine WS_2 or rGO. Meanwhile, the matching impedance values with the comparison rGO > WS_2 > WS_2–rGO are presented in Fig. 7. The results are consistent with the RL results shown in Fig. 5, indicating that the WS_2–rGO heterostructure nanosheets exhibit advantages in impedance matching.

Figure 5 shows that the RL of pristine rGO or WS_2 is relatively weak when the thickness is small; meanwhile, the RL of WS_2–rGO heterostructure nanosheets increased with

decreasing thickness. Moreover, the coupling between WS$_2$ and rGO also resulted in a shift of the effective absorption band to the low-frequency region. These unique properties enabled the WS$_2$–rGO heterostructure nanosheets to achieve the unique features of strong absorption, small thickness, and lightweight. The AFM image further characterizes the thickness of the heterostructure, as shown in Fig. S5 of the supplementary information. Compared to that of WS$_2$ nanosheets, the thickness of the heterostructure increased, although the overall thickness was approximately 50 nm. This establishes that the WS$_2$–rGO heterostructure nanosheets prepared were particularly thin material. Figure S6 displays a piece of sample made from the as-prepared WS$_2$–rGO heterostructure nanosheets; it is placed on a blade of *Setaria viridis*. The fluff of *Setaria viridis* did not exhibit apparent bending; moreover, the sample did not
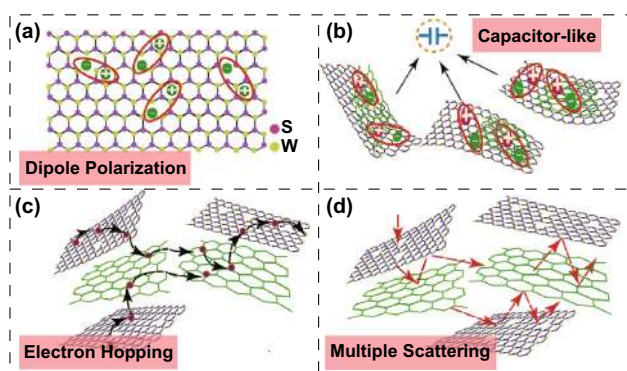
fall. This verified the remarkable lightweight features of the WS$_2$–rGO heterostructure nanosheet used as microwave absorbent.

In order to explain the absorption properties of and defect formation in the WS$_2$–rGO heterostructure nanosheets, electron paramagnetic resonance (EPR) and photoluminescence (PL) measurements were performed (Fig. S7). Figure S7A shows that the PL peaks for WS$_2$, rGO, and the WS$_2$–rGO heterostructure nanosheets are located at 388.2, 392.1, and 394.6 nm, respectively. The small luminescence intensity of tungsten disulfide indicates the presence of numerous defects [62]. Compared with that of WS$_2$ or rGO, the PL peak for the WS$_2$–rGO heterostructure nanosheets exhibits a significant blueshift; this is owing to the reduced number of layers of the WS$_2$–rGO heterostructure nanosheets after the heterostructurization. The PL peak intensity for the WS$_2$–rGO heterostructure nanosheets is higher than that of WS$_2$ or rGO; this indicates that the carrier recombination was strong and that the defect concentration could have been increased. Because the defect sites were more likely to become recombination centers, the charge recombination aggravated. Therefore, the PL peak intensity of the heterostructure increased. Figure S7B shows the EPR spectrum of the WS$_2$–rGO heterostructure nanosheets at room temperature. The signal appears at the vicinity of the magnetic field of 3513 G ($g \approx 1.9$). The narrow signal peaks could be related to the presence of S (Vs) vacancies. The large peak intensity established that the S vacancies had a large defect concentration; this again established that the WS$_2$–rGO heterostructure nanosheets had a large number of defects, resulting in dipole polarization losses.
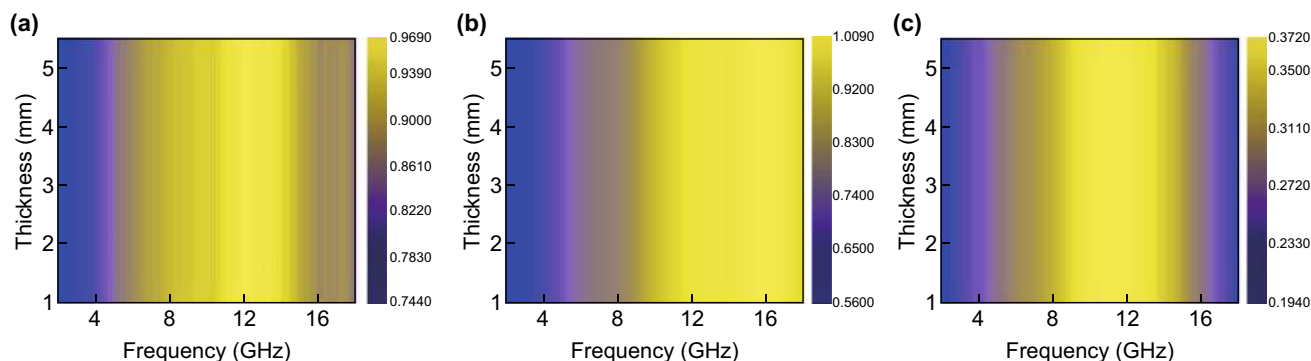

Fig. 6 Synergistic mechanisms responsible for the superior microwave absorption properties of the proposed WS$_2$–rGO heterostructure nanosheet absorbent: **a** dipole polarization. **b** Interfacial polarization. **c** Electron hopping. **d** Multiple scattering of incident microwave

Fig. 7 Calculated delta value maps of **a** rGO, **b** WS$_2$, and **c** WS$_2$–rGO
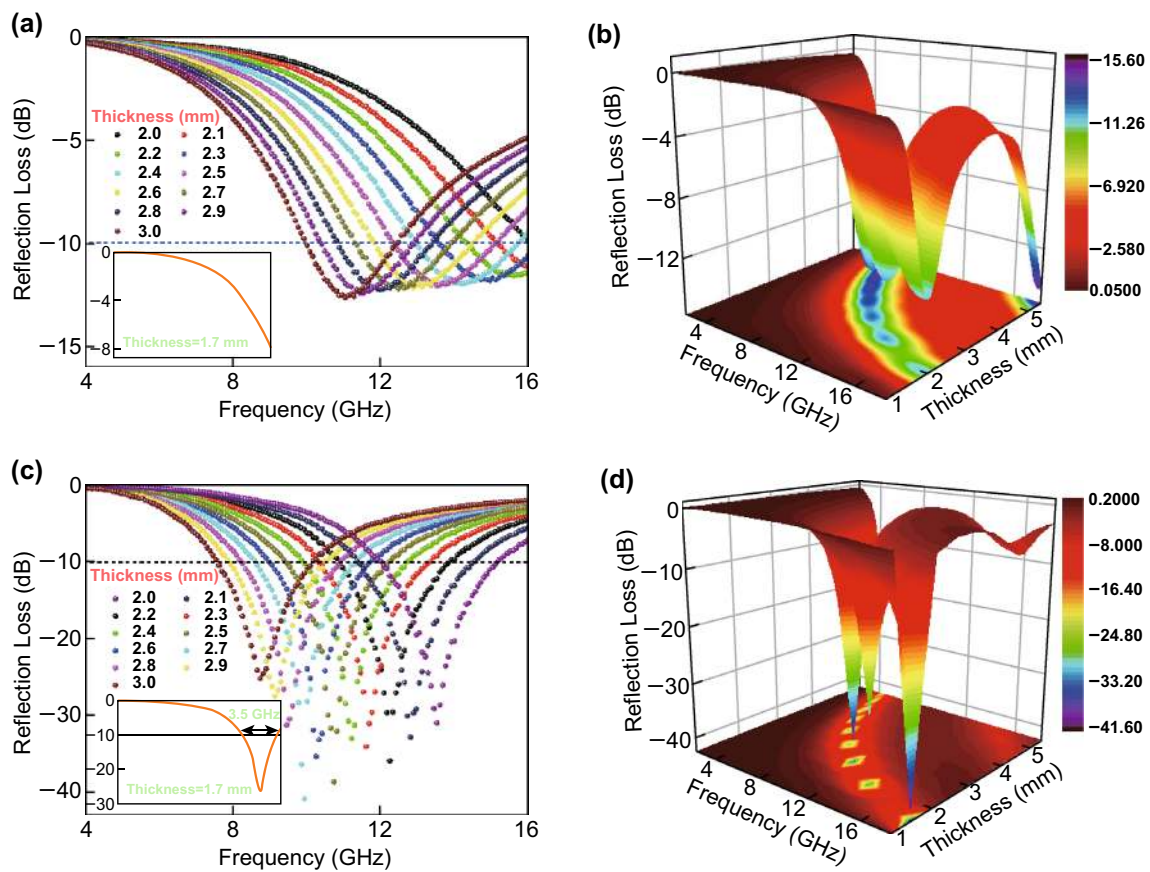
Fig. 8 **a**, **c** Reflection loss profiles and **b**, **d** 3D maps of RL of pristine WS_2 microwave absorbent at thickness of 2.0–3.0 mm (**a**, **b**) and WS_2–rGO heterostructure nanosheet absorbent at thickness of 2.0–3.0 mm (**c**, **d**). The insets in panels **a** and **e** show the RL curves of the pristine WS_2 and the WS_2–rGO heterostructure nanosheet absorbents at a thickness of 1.7 mm

In addition, UV–Vis and BET tests were carried out to characterize the porous WS_2–rGO heterostructure structure and to further demonstrate the microwave absorbing properties. As shown in Fig. S8A, the absorption spectrum of WS_2–rGO heterostructure nanosheets exhibits a distinct absorption peak in the wavelength range of 190–400.7 nm. This absorption peak exhibits a significant blueshift as compared to the characteristic absorption peak at 920 nm (with a forbidden band width of 1.35 eV) for the tungsten disulfide bulk material; this is apparently caused by the quantum confinement effect. The strong absorption strength of the WS_2–rGO heterostructure nanosheets at 190–400.7 nm could have been owing to the high specific surface area of these nanosheets; this was demonstrated by the nitrogen adsorption test. The BET surface areas and pore size distribution curves of the WS_2–rGO heterostructure nanosheets were obtained by

nitrogen adsorption–desorption measurements, as shown in Fig. S8B. The isotherm is of type IV according to the Brunauer–Deming–Deming–Teller classification. Furthermore, the shapes of the hysteresis loops in the P/P_0 range of 0.4–1.0 are of type H3, which indicate the formation of porous structures in the samples. The pore size distribution curves indicate that the samples exhibited wide pore size distributions (3–30 nm) with a main pore size of 3.409 nm; this verifies the presence of mesopores in the samples. The BET-specific surface areas of the WS_2–rGO heterostructure nanosheets were 72.916 $m^2 g^{-1}$. The illustrations in Fig. 5a, c, e show the models of preparation of rGO, WS_2, and the WS_2–rGO heterostructure nanosheets, respectively. The unique processing condition produced tungsten disulfide WS_2–rGO hybrid material with remarkable performance, ultra-lightweight, ultra-small thickness, and high specific surface. This indicates that the WS_2–rGO heterostructure

nanosheets could have been porous and have had a high specific surface area, providing more spaces for multiple reflections and scattering of electromagnetic waves. The porous structure also facilitated the formation of a uniform complicate conductive network, resulting in remarkable electromagnetic wave absorption in the WS_2–rGO heterostructure nanosheets.

Figure 8 shows the RL of WS_2 and the WS_2–rGO heterostructure nanosheets with thicknesses of 2.0–3.0 mm. The maximum effective bandwidth of the WS_2–rGO heterostructure nanosheet absorbent is calculated to be 3.5 GHz at a rather small thickness of 1.7 mm, as shown in the inset of Fig. 8c; meanwhile, the effective bandwidth of pristine WS_2 at this thickness is zero (inset of Fig. 8a). It is further observed in Fig. 8 that with a relatively small thickness of 2.0–3.0 mm, the pristine WS_2 exhibited low microwave absorption performance as compared to the WS_2–rGO heterostructure nanosheets. The maximum RL of the WS_2–rGO nanosheets could have been -41.5 dB at a thickness of 2.7 mm; this indicates that the heterostructurization of WS_2 with rGO is an efficient method for improving the absorbing properties (*i.e.,* RL). The aforementioned results thus indicate that WS_2–rGO heterostructure nanosheets exhibit significant potential for applications as novel high-performance microwave absorbents because of their facile one-pot synthesis route, lightweight, small thickness, low cost, and corrosion and oxidation resistance, in conjunction with their significantly enhanced RL and effective bandwidth.

4 Conclusions

In summary, well-defined WS_2–rGO heterostructure nanosheets were directly synthesized via a facile one-step hydrothermal approach; moreover, their microwave absorption performance was investigated. Significantly enhanced absorption was observed in the WS_2–rGO heterostructure nanosheet absorbent, as reflected by the high RL and extended effective absorption bandwidth; this could be attributed to the interfacial dielectric coupling at the well-defined WS_2–rGO interfaces constructed by the introduction of rGO. In particular, it is observed that the absorber made from the WS_2–rGO heterostructure nanosheets of thickness 2.7 mm achieved the maximum RL of –41.5 dB at 9.5 GHz. More remarkably, a large effective absorption bandwidth of

3.5 GHz could be realized by the heterostructure absorber of thickness approximately 1.7 mm. In addition, the effective bandwidth for the WS_2–rGO heterostructure nanosheet absorber could be further adjusted from 18 GHz to a low-frequency band by adding rGO. Because of their attractive microwave absorption properties as well as their features of facile synthesis route, small thickness, and lightweight, the WS_2–rGO heterostructure nanosheets are considered to be potential lightweight and wide-frequency microwave absorption materials.

References

1. Q. Liu, Q. Cao, H. Bi, C. Liang, K. Yuan, W. She, Y. Yang, R. Che, CoNi@ SiO_2@TiO_2 and CoNi@ Air@TiO_2 microspheres with strong wideband microwave absorption. Adv. Mater. **28**(3), 486–490 (2016). https://doi.org/10.1002/adma.201503149

2. H. Lv, Z. Yang, S.J.H. Ong, C. Wei, H. Liao, S. Xi, Y. Du, G. Ji, Z.J. Xu, A flexible microwave shield with tunable frequency-transmission and electromagnetic compatibility. Adv. Funct. Mater. **29**(14), 1900163 (2019). https://doi.org/10.1002/adfm.201900163

3. X. Yan, D. Xue, Fabrication and microwave absorption properties of $Fe_{0.64}Ni_{0.36}$–$NiFe_2O_4$ nanocomposite. Nano-Micro Lett. **4**(3), 176–179 (2012). https://doi.org/10.1007/BF03353710

4. M.S. Cao, W.L. Song, Z.L. Hou, B. Wen, J. Yuan, The effects of temperature and frequency on the dielectric properties, electromagnetic interference shielding and microwave-absorption of short carbon fiber/silica composites. Carbon **48**(3), 788–796 (2010). https://doi.org/10.1016/j.carbon.2009.10.028

5. H. Lv, Z. Yang, P.L. Wang, G. Ji, J. Song, L. Zheng, H. Zeng, Z.J. Xu, A voltage-boosting strategy enabling a low-frequency,

flexible electromagnetic wave absorption device. Adv. Mater. **30**(15), 1706343 (2018). https://doi.org/10.1002/adma.201706343

6. G. Wang, Z. Gao, S. Tang, C. Chen, F. Duan et al., Microwave absorption properties of carbon nanocoils coated with highly controlled magnetic materials by atomic layer deposition. ACS Nano **6**(12), 11009–11017 (2012). https://doi.org/10.1021/nn304630h

7. C. Chen, J. Xi, E. Zhou, L. Peng, Z. Chen, C. Gao, Porous graphene microflowers for high-performance microwave absorption. Nano-Micro Lett. **10**(2), 26 (2018). https://doi.org/10.1007/s40820-017-0179-8

8. C. Li, Q. Cao, F. Wang, Y. Xiao, Y. Li, J. Delaunay, H. Zhu, Engineering graphene and TMDs based van der Waals heterostructures for photovoltaic and photoelectrochemical solar energy conversion. Chem. Soc. Rev. **47**(13), 4981–5037 (2018). https://doi.org/10.1039/C8CS00067K

9. P. Liu, Y. Huang, J. Yan, Y. Yang, Y. Zhao, Construction of CuS nanoflakes vertically aligned on magnetically decorated graphene and their enhanced microwave absorption properties. ACS Appl. Mater. Interfaces **8**(8), 5536–5546 (2016). https://doi.org/10.1021/acsami.5b10511

10. A. Gupta, T. Sakthivel, S. Seal, Recent development in 2D materials beyond graphene. Prog. Mater. Sci. **73**, 44–126 (2015). https://doi.org/10.1016/j.pmatsci.2015.02.002

11. X.H. Li, J. Feng, Y.P. Du, J.T. Bai, H.M. Fan, H.L. Zhang, H. Peng, F.S. Li, One-pot synthesis of $CoFe_2O_4$/graphene oxide heterostructures and their conversion into FeCo/graphene heterostructures for lightweight and highly efficient microwave absorber. J. Mater. Chem. A **3**(10), 5535–5546 (2015). https://doi.org/10.1039/c4ta05718j

12. P. Liu, M. Yang, S. Zhou, Y. Huang, Y. Zhu, Hierarchical shell-core structures of concave spherical NiO nanospines@carbon for high performance supercapacitor electrodes. Electrochim. Acta **294**, 383–390 (2018). https://doi.org/10.1016/j.electacta.2018.10.112

13. D. Chen, Z. Wan, X. Chen, Y. Yuan, J. Zhong, Large-scale room-temperature synthesis and optical properties of perovskite-related Cs4PbBr 6 fluorophores. J. Mater. Chem. C **4**(45), 6362–6370 (2016). https://doi.org/10.1039/C6TC04036E

14. X. Zhang, Y. Huang, P. Liu, Enhanced electromagnetic wave absorption properties of poly(3,4-ethylenedioxythiophene) nanofiber-decorated graphene sheets by non-covalent interactions. Nano-Micro Lett. **8**(2), 131–136 (2016). https://doi.org/10.1007/s40820-015-0067-z

15. H. Yu, T. Wang, B. Wen, M. Lu, Z. Xu et al., Graphene/polyaniline nanorod arrays: synthesis and excellent electromagnetic absorption properties. J. Mater. Chem. **22**(40), 21679–21685 (2012). https://doi.org/10.1039/C2JM34273A

16. X.J. Zhang, G.S. Wang, W.Q. Cao, Y.Z. Wei, M.S. Cao, L. Guo, Enhanced microwave absorption property of reduced graphene oxide (RGO)-$MnFe_2O_4$ nanocomposites and polyvinylidene fluoride. RSC Adv. **6**(10), 7471–7478 (2014). https://doi.org/10.1021/am500862g

17. Z. Yin, H. Li, H. Li, L. Jiang, Y. Shi, Y. Sun, Single-layer MoS_2 phototransistors. ACS Nano **6**(1), 74–80 (2012). https://doi.org/10.1021/nn2024557

18. M. Zong, Y. Huang, N. Zhang, H.W. Wu, Facile synthesis of RGO/Fe_3O_4/Ag composite with high microwave absorption capacity. Mater. Lett. **111**(15), 188–191 (2013). https://doi.org/10.1016/j.matlet.2013.08.076

19. H. Zeng, J. Dai, W. Yao, D. Xiao, X. Cui, Valley polarization in MoS_2 monolayers by optical pumping. Nat. Nanotechnol. **7**(8), 490–493 (2012). https://doi.org/10.1038/nnano.2012.95

20. M.Q. Ning, M.M. Lu, J.B. Li, Z. Chen, Y.K. Dou, C.Z. Wang, F. Rehman, M.S. Cao, H.B. Jin, Two-dimensional nanosheets of MoS_2: a promising material with high dielectric properties and microwave absorption performance. Nanoscale **7**(38), 15734–15740 (2015). https://doi.org/10.1039/c5nr04670j

21. L. Bai, Y. Wang, F. Li, D. An, Z. Zhang, Y. Liu, Enhanced electromagnetic wave absorption properties of MoS_2-graphene heterostructure nanosheets prepared by a hydrothermal method. J. Sol-Gel Sci. Technol. **84**(1), 104–109 (2017). https://doi.org/10.1007/s10971-017-4478-9

22. D.Q. Zhang, Y.X. Jia, J.Y. Cheng, S.M. Chen, J.X. Chai et al., High-performance microwave absorption materials based on MoS_2-graphene isomorphic hetero-structures. J. Alloys Compd. **758**, 62–71 (2018). https://doi.org/10.1016/j.jallcom.2018.05.130

23. Y. Sun, W. Zhong, Y. Wang, X. Xu, T. Wang, L. Wu, Y. Du, MoS_2 based mixed-dimensional van der Waals heterostructures: a new platform for excellent and controllable microwave absorption performance. ACS Appl. Mater. Interfaces **9**(39), 34243–34255 (2017). https://doi.org/10.1021/acsami.7b10114

24. M.S. Cao, J.C. Shu, X.X. Wang, X. Wang, M. Zhang, H.J. Yang, X.Y. Fang, J. Yuan, Electronic structure and electromagnetic properties for 2D electromagnetic functional materials in gigahertz frequency. Ann. Phys. **531**(4), 1800390 (2019). https://doi.org/10.1002/andp.201800390

25. C.S. Rout, P.D. Joshi, R.V. Kashid, D.S. Joag, M.A. More, A.J. Simbeck, M. Washington, S.K. Nayak, D.J. Late, Superior field emission properties of layered WS2–rGO nanocomposites. Sci. Rep. **3**(7476), 3282 (2013). https://doi.org/10.1038/srep03282

26. J. Zhang, Q. Wang, L. Wang, X.A. Li, W. Huang, Layer-controllable WS2-reduced graphene oxide heterostructure nanosheets with high electrocatalytic activity for hydrogen evolution. Nanoscale **7**, 10391–10397 (2015). https://doi.org/10.1039/c5nr01896j

27. R. Bhandavat, L. David, G. Singh, Synthesis of surface-functionalized WS_2 nanosheets and performance as Li-ion battery anodes. J. Phys. Chem. Lett. **3**(11), 1523–1530 (2012). https://doi.org/10.1021/jz300480w

28. H. Zhao, Y. Cheng, W. Liu, L. Yang, B. Zhang, L.P. Wang, G.B. Ji, J. Xu, Biomass-derived porous carbon-based nanostructures for microwave absorption. Nano-Micro Lett. **11**, 24 (2019). https://doi.org/10.1007/s40820-019-0255-3

29. H. Sun, R.C. Che, X. You, Y.S. Jiang, Z.B. Yang, J. Deng, Cross-stacking aligned carbon-nanotube films to tune

microwave absorption frequencies and increase absorption intensities. Adv. Mater. **26**(48), 8120–8125 (2014). https://doi.org/10.1002/adma.201403735

30. P. Saini, V. Choudhary, B.P. Singh, R.B. Mathur, S.K. Dhawan, Enhanced microwave absorption behavior of polyaniline-CNT/polystyrene blend in 12.4–18.0 GHz range. Synth. Met. **161**(15), 1522–1526 (2011). https://doi.org/10.1016/j.synthmet.2011.04.033

31. D.C. Tiwari, P. Dipak, S.K. Dwivedi, T.C. Shami, P. Dwivedi, Py/TiO₂ (np)/CNT polymer nanocomposite material for microwave absorption. J. Mater. Sci.: Mater. Electron. **29**(2), 1643–1650 (2018). https://doi.org/10.1007/s10854-017-8076-y

32. T.K. Zhao, C.L. Hou, H.Y. Zhang, R.X. Zhu, S.F. She, J.G. Wang, T.H. Li, Z.F. Liu, B.Q. Wei, Electromagnetic wave absorbing properties of amorphous carbon nanotubes. Sci. Rep. **4**, 5619 (2014). https://doi.org/10.1038/srep05619

33. Y. Zhang, Y. Huang, T.F. Zhang, H.C. Chang, P.S. Xiao, H.H. Chen, Z.Y. Huang, Y.S. Chen, Broadband and tunable high-performance microwave absorption of an ultralight and highly compressible graphene foam. Adv. Mater. **27**(12), 2049–2053 (2015). https://doi.org/10.1002/adma.201405788

34. H. Wang, Y.Y. Dai, D.Y. Geng, S. Ma, D. Li, J. An, J. He, W. Liu, Z.D. Zhang, Co$_x$Ni$_{100-x}$ nanoparticles encapsulated by curved graphite layers: controlled in situ metal-catalytic preparation and broadband microwave absorption. Nanoscale **7**(41), 17312–17319 (2015). https://doi.org/10.1039/c5nr03745j

35. T. Liu, X.B. Xie, Y. Pang, S. Kobayashi, Co/C nanoparticles with low graphitization degree: a high performance microwave absorbing material. J. Mater. Chem. C **4**(8), 1727–1735 (2016). https://doi.org/10.1039/C5TC03874J

36. C. Chen, J.B. Xi, E.Z. Zhou, L. Peng, Z.C. Chen, C. Gao, Porous graphene microflowers for high-performance microwave absorption. Nano-Micro Lett. **10**(2), 26 (2018). https://doi.org/10.1007/s40820-017-0179-8

37. L. Wang, Y. Huang, C. Li, J. Chen, X. Sun, A facile one-pot method to synthesize a three-dimensional graphene@carbon nanotube composite as a high-efficiency microwave absorber. Phys. Chem. Chem. Phys. **17**(3), 2228–2234 (2015). https://doi.org/10.1039/c4cp04745a

38. X.B. Li, S.W. Yang, J. Sun, P. He, X.P. Pu, G.Q. Ding, Enhanced electromagnetic wave absorption performances of Co₃O₄ nanocube/reduced graphene oxide composite. Synth. Met. **194**, 52–58 (2014). https://doi.org/10.1016/j.synthmet.2014.04.012

39. X. Ding, Y. Huang, S. Li, N. Zhang, J. Wang, 3D architecture reduced graphene oxide–MoS₂ composite: preparation and excellent electromagnetic wave absorption performance. Compos. A **90**, 424–432 (2016). https://doi.org/10.1016/j.compositesa.2016.08.006

40. S. Liu, B. Shen, Y. Niu, M. Xu, Fabrication of WS₂-nanoflowers@rGO composite as an anode material for enhanced electrode performance in lithium-ion batteries. J. Colloid Interface Sci. **488**, 20–25 (2017). https://doi.org/10.1016/j.jcis.2016.10.083

41. T.A. Shifa, F. Wang, Z. Cheng, X. Zhan, Z. Wang, K. Liu, M. Safdaret, L. Sun, L. He, A vertical-oriented WS₂ nanosheet sensitized by graphene: an advanced electrocatalyst for hydrogen evolution reaction. Nanoscale **7**, 14760–14765 (2015). https://doi.org/10.1039/C5NR03704B

42. N.T. Shelke, B.R. Karche, Hydrothermal synthesis of WS₂/RGO sheet and their application in UV photodetector. J. Alloys Compd. **653**, 298–303 (2015). https://doi.org/10.1016/j.jallcom.2015.08.255

43. B. Späth, F. Kopnov, H. Cohen, A. Zak, A. Moshkovich, L. Rapoport et al., X-ray photoelectron spectroscopy and tribology studies of annealed fullerene-like WS₂ nanoparticles. Phys. Status Solidi **245**(9), 51–59 (2010). https://doi.org/10.1002/pssb.200779531

44. Y. Wang, D. Chen, X. Yin, P. Xu, F. Wu, M. He, Heterostructure of MoS₂ and reduced graphene oxide: A lightweight and broadband electromagnetic wave absorber. ACS Appl. Mater. Interfaces **7**(47), 26226–26234 (2015). https://doi.org/10.1021/acsami.5b08410

45. Y.L. Chen, L. Song, H. Guo, Hydrothermal synthesis of tungsten disulfide/graphene composites and their oxygen reduction properties. J. Inorg. Chem. **32**, 633–640 (2016). https://doi.org/10.11862/CJIC.2016.073

46. X.X. Wang, T. Ma, J.C. Shu, M.S. Cao, Confinedly tailoring Fe₃O₄ clusters-NG to tune electromagnetic parameters and microwave absorption with broadened bandwidth. Chem. Eng. J. **332**, 321–330 (2017). https://doi.org/10.1016/j.cej.2017.09.101

47. W.L. Song, M.S. Cao, Z.L. Hou, M.M. Lu, C.Y. Wang, J. Yuan, L.Z. Fan, Beta-manganese dioxide nanorods for sufficient high-temperature electromagnetic interference shielding in X-band. Appl. Phys. A **116**(4), 1779–1783 (2014). https://doi.org/10.1007/s00339-014-8327-1

48. J.V. Mantese, A.L. Micheli, D.F. Dungan, R.G. Geyer, J. Baker-Jarvis, J. Grosvenor, Applicability of effective medium theory to ferroelectric/ferrimagnetic composites with composition and frequency–dependent complex permittivities and permeabilities. J. Appl. Phys. **79**(3), 1655–1660 (1996). https://doi.org/10.1063/1.361010

49. H.L. Zhu, Y.J. Bai, R. Liu, N. Lun, Y.X. Qi, F.D. Han, J.Q. Bi, Synthesis of one-dimensional MWCNT/SiC porous nanocomposites with excellent microwave absorption properties. J. Mater. Chem. **21**(35), 13581–13587 (2011). https://doi.org/10.1039/C1JM11747E

50. P.B. Liu, Y. Huang, X. Zhang, NiFe₂O₄ clusters on the surface of reduced graphene oxide and their excellent microwave absorption properties. Mater. Lett. **112**(12), 117–120 (2013). https://doi.org/10.1016/j.matlet.2013.08.126

51. D.Q. Zhang, J.X. Chai, J.Y. Cheng, Y.X. Jia, X.Y. Yang, H. Wang, Highly efficient microwave absorption properties and broadened absorption bandwidth of MoS₂-iron oxide heterostructures and MoS₂-based reduced graphene oxide heterostructures with hetero-structures. Appl. Surf. Sci. **462**, 872–882 (2018). https://doi.org/10.1016/j.apsusc.2018.08.152

52. N. Yousefi, X.Y. Sun, X.Y. Lin, X. Shen, J.J. Jia et al., Highly aligned graphene/polymer nanocomposites with excellent

dielectric properties for high-performance electromagnetic interference shielding. Adv. Mater. **26**(31), 5480–5487 (2014). https://doi.org/10.1002/adma.201305293

53. P. Liu, Y. Zhang, J. Yan, Y. Huang, L. Xia, Z. Guang, Synthesis of lightweight N-doped graphene foams with open reticular structure for high-efficiency electromagnetic wave absorption. Chem. Eng. J. **368**, 285–298 (2019). https://doi.org/10.1016/j.cej.2019.02.193

54. M.S. Cao, C. Han, X.X. Wang, M. Zhang, Y.L. Zhang, J.C. Shu, H.J. Yang, X.Y. Fang, J. Yuan, Graphene nanoheterostructure: excellent electromagnetic properties for electromagnetic wave absorbing and shielding. J. Mater. Chem. C **6**, 4586–4602 (2018). https://doi.org/10.1039/c7tc05869a

55. X.M. Zhang, G.B. Jin, W. Liu, X.X. Zhang, Q.W. Gao, Y.C. Li, Y.W. Du, A novel Co/TiO_2 nanocomposite derived from a metal–organic framework: synthesis and efficient microwave absorption. J. Mater. Chem. C **4**(9), 1860–1870 (2016). https://doi.org/10.1039/C6TC00248J

56. W. Liu, Q.W. Shao, G.B. Ji, X.H. Liang, B. Quan, Y.W. Du, Metal–organic-frameworks derived porous carbon-wrapped Ni composites with optimized impedance matching as excellent lightweight electromagnetic wave absorber. Chem. Eng. J. **313**, 734–744 (2017). https://doi.org/10.1016/j.cej.2016.12.117

57. J.P. Wang, J. Wang, R. Xu, Y. Sun, B. Zhang, W. Chen, T. Wang, S. Yang, Enhanced microwave absorption properties of epoxy composites reinforced with $Fe_{50}Ni_{50}$-functionalized graphene. J. Alloys Compd. **653**, 14–21 (2015). https://doi.org/10.1016/j.jallcom.2015.08.278

58. B. Quan, X. Liang, G. Ji, J. Ma, P. Ouyang, H. Gong, G. Xu, Y. Du, Strong electromagnetic wave response derived from the construction of dielectric/magnetic media heterostructure and multiple interfaces. ACS Appl. Mater. Interfaces **9**(11), 9964–9974 (2017). https://doi.org/10.1021/acsami.6b15788

59. S. Dong, W. Zhang, X. Zhang, P. Hu, J. Han, Designable synthesis of core-shell SiCw@C heterostructures with thickness-dependent electromagnetic wave absorption between the whole X-band and Ku-band. Chem. Eng. J. **354**, 767–776 (2018). https://doi.org/10.1016/j.cej.2018.08.062

60. R. Mehmood, S. Nadeem, S. Masood, Effects of transverse magnetic field on a rotating micropolar fluid between parallel plates with heat transfer. J. Magn. Magn. Mater. **401**(3), 1006–1014 (2016). https://doi.org/10.1016/j.jmmm.2015.10.102

61. Y. Cheng, Z.Y. Li, Y. Li, S.S. Dai, G.B. Ji, H.Q. Zhao, J.M. Cao, Y.W. Du, Rationally regulating complex dielectric parameters of mesoporous carbon hollow spheres to carry out efficient microwave absorption. Carbon **127**, 643–652 (2018). https://doi.org/10.1016/j.carbon.2017.11.055

62. M.O. Valappil, A. Anil, M. Shaijumon, V.K. Pillai, S. Alwarappan, A single-step electrochemical synthesis of luminescent WS_2 quantum dots. Chem. Eur. J. **23**, 9144–9148 (2017). https://doi.org/10.1002/chem.201701277